Remote Sensing of Environment 137 (2013) 31–42

Contents lists available at SciVerse ScienceDirect

Remote Sensing of Environment

journal homepage: www.elsevier.com/locate/rse

Remote sensing of transpiration and heat fluxes using multi-angle observations

Thomas Hilker [a,*], Forrest G. Hall [b], Nicholas C. Coops [c], James G. Collatz [b], T. Andrew Black [d], Compton J. Tucker [b], Piers J. Sellers [b], Nicholas Grant [d]

[a] Oregon State University, College of Forestry, 231 Peavy Hall, Corvallis OR 97331, USA
[b] NASA Goddard Space Flight Center, 8800 Greenbelt Road, Greenbelt, MD 20771, USA
[c] Faculty of Forest Resources Mgmt, University of British Columbia, 2424 Main Mall, Vancouver, BC V6T1Z4, Canada
[d] Faculty of Land and Food Systems, University of British Columbia, 2357 Main Mall, Vancouver, BC V6T1Z4, Canada

ARTICLE INFO

Article history:
Received 13 January 2013
Received in revised form 23 May 2013
Accepted 25 May 2013
Available online 28 June 2013

Keywords:
Multi-angle remote sensing AMSPEC
GPP
Transpiration
Ball–Berry relationship
Stomatal conductance

ABSTRACT

Surface energy balance is a major determinant of land surface temperature and the Earth's climate. To date, there is no approach that can produce effective, physically consistent, global and multi-decadal energy–water flux data over land. Net radiation (R_n) can be quantified regionally using satellite retrievals of surface reflectance and thermal emittance with errors <10%. However, consistent, useful retrieval of latent heat flux (λE) from remote sensing is not yet possible. In theory, λE could be inferred as a residual of R_n, ground heat (G) and sensible heat (H) fluxes (R_n–H–G). However, large uncertainties in remote sensing of both H and G result in low accuracies for λE. Where vegetation is the dominant surface cover, λE is largely driven by transpiration of intercellular water through leaf stomata during the photosynthetic uptake of carbon. In these areas, satellite retrievals of photosynthesis (GPP) could be used to quantify transpiration rates through stomatal conductance. Here, we demonstrate how remote sensing of GPP could be applied to obtain λE from passive optical measurements of vegetation leaf reflectance related to the photosynthetic rate independent of knowledge of H, R_n and G. We validate the algorithm using five structurally and physiologically diverse eddy flux sites in western and central Canada. Results show that transpiration and H were accurately predicted from optical data and highly significant relationships were found between the energy budget obtained from eddy flux measurements and remote sensing ($0.64 \leq r^2 \leq 0.85$). We conclude that spaceborne estimates of GPP could significantly improve not only estimates of the carbon balance but also the energy balance over land.

1. Introduction

Terrestrial vegetation plays a significant role in the re-distribution of moisture and heat in the surface boundary layer (Bastiaanssen, Menenti, Feddes & Holtslag, 1998) and the surface energy balance of the planet. Thermal equilibrium at the Earth's land surface is maintained through a combination of thermodynamic and physiological processes (Hall et al., 1991) as the energy of the net radiation (R_N) absorbed by the surface is balanced by sensible (H), latent (λE), and ground heat fluxes (G) from the surface back to the atmosphere (Hall et al., 1991; Sellers, Randall, et al., 1996).

$$R_N = H + \lambda E + G. \quad (1)$$

Stand level observations of λE, H and G have been available from eddy covariance (EC) towers (Kidston et al., 2010) and soil heat flux plates (Garzoli et al., 1971) for quite some time. However, scaling these components to landscape and global levels remains challenging. First, discrete observations often fail to adequately reflect the spatial heterogeneity in land cover, stand age and soil type (Goulden et al., 1996) and second, eddy covariance measurements tend to underestimate heat fluxes (Aubinet et al., 2000) as large eddies are often under-sampled by micro-meteorological observations. These errors, when scaled, may propagate across the landscape (Kidston et al., 2010).

The sensible heat transfer of vegetation is mostly driven by the temperature difference above and within the canopy air space (Hall et al., 1992; Sellers, Randall, et al., 1996). Early work during FIFE (First ISLSCP Field Experiment, Hall, & Sellers, 1995) has shown that remotely sensed measures of thermal radiation can be used to derive canopy aerodynamic temperatures via the Stefan–Boltzmann law (Anderson et al., 2008; Choudhury et al., 1986). Required assumptions about the emissivity of the canopy surface, however, can produce sizeable errors (>30%) in remotely sensed sensible heat flux (Hall et al., 1992) and performance depends on the degree to which calibration targets are available (Bastiaanssen, Menenti, Feddes & Holtslag, 1998; Bastiaanssen, Pelgrum, et al., 1998).

* Corresponding author. Tel.: +1 541 737 2608.
E-mail address: thomas.hilker@oregonstate.edu (T. Hilker).

0034-4257/$ – see front matter © 2013 Elsevier Inc. All rights reserved.
http://dx.doi.org/10.1016/j.rse.2013.05.023

Latent heat exchange over vegetated surfaces is composed of (1) evaporation of water from aboveground, free water surfaces and soils and (2) transpiration of intercellular water through leaf stomata during the photosynthetic uptake of carbon. In vegetated regions, transpiration is the dominant source of water flux during most of the growing season (Collatz et al., 1991; Hall et al., 1991). Transpiration is directly linked to photosynthetic rate (Collatz et al., 1991; Hall et al., 1991) since the vapor-saturated stomatal chambers release water vapor when stomata are open to take up carbon dioxide during photosynthesis. As a result, λE can be obtained either from gross photosynthesis (GPP), or as a residual of H, G and R_n by closing the surface energy balance (Bastiaanssen, Menenti, Feddes & Holtslag, 1998). Several models exist to determine λE using residual approaches; however uncertainties in both H and G result in accuracies of λE significantly lower than those of the other energy balance components. In addition to uncertainties in H, G is a function of both surface and subsurface soil temperature as well as the thermal conductance of the surface layer, which is not directly available over larger areas.

Coupled models to estimate λE from photosynthesis exist (Anderson et al., 2008) and have been embedded within a surface energy and water balance framework (Baldocchi & Wilson, 2001; Leuning, 1990; Norman et al., 2003; Sellers, Randall, et al., 1996). These models are based on the relation between leaf gross photosynthesis (A) and leaf stomatal conductance (g_s) based on physiological concepts developed by Farquhar et al. (1980), Collatz et al. (1990) and models of stomatal resistance (Ball, 1988; Jarvis, 1976; Leuning, 1990).

$$g_s = m\frac{Ah_s}{c_s} + b \tag{2}$$

where A is the rate of leaf CO_2 uptake or Gross Primary Production (GPP), h_s is the relative humidity and c_s is the CO_2 mole fraction (375 mol mol^{-1}) measured within the canopy layer (Collatz et al., 1991). m and b are, respectively, slope and minimum conductance obtained from empirical data (Collatz et al., 1991). While this technique has been widely applied, it is currently limited by our ability to accurately determine GPP over large areas (dePury & Farquhar, 1997). Enzyme kinetic models of GPP have been used extensively in land-surface and climate models (Dickinson et al., 1998; Sellers, Los, et al., 1996), but require a large number of input parameters (Houborg & Soegaard, 2004) that are not typically available at the landscape level. Light limited approaches estimate GPP using climatic drivers that are available from remote sensing, but make no attempt to model the underlying biophysical and biochemical processes. To date, neither enzyme kinetics nor light-limited models are capable of estimating GPP across an array of diverse sites within the observed uncertainty ranges (Schaefer et al., 2012).

Recently, Hall et al. (2008) developed a new approach to determine canopy GPP based on the Monteith (1972) approach from multi-angular remote sensing of photosynthetic light use efficiency (ε): Vegetation light-use efficiency is controlled by the xanthophyll cycle, a biochemical mechanism balancing light-use and absorption in plants. This cycle is triggered by a conversion of the xanthophyll cycle pigment violaxanthin to zeaxanthin (Demmig-Adams & Adams, 1996), a change that is associated with an absorption band at 531 nm and quantifiable using the photochemical reflectance index (PRI) (Gamon, 1992). The biophysical relationship between PRI and ε has been known for two decades, however, extraneous effects of canopy structure, view-observer geometry and vegetation type have so far hampered its use as a measure of photosynthetic down-regulation. New research using multi-angle observations of PRI (Hall et al., 2008), has demonstrated that changes in the xanthophyll cycle can be robustly quantified across ecosystems when relating directional change in PRI to the shaded–sunlit canopy fraction (α_s). Theoretical (Hall et al., 2011) and experimental (Hilker, Hall, et al., 2010; Hilker et al., 2011) research has provided a solid basis of this technique as a measure of instantaneous ε across terrestrial vegetation types (Hall et al., 2011).

The objective of this study is to demonstrate that remotely sensed estimates of ε could allow spatially explicit information also of λE, which should considerably improve current models of the surface energy balance. For instance, when combined with a data assimilation approach (Hall et al., 2012b; Hilker, Nesic, Coops & Lessard, 2010) spatially continuous estimates of GPP could be extrapolated in time and therefore also yield temporally and spatially continuous estimates of λE.

2. Approach

2.1. Latent heat transfer

Total water flux from a surface is the sum of evaporation and transpiration. The driving force to remove water vapor from the evaporating surface is the difference between the water vapor pressure at the surface and the saturated vapor pressure of the surrounding canopy air space at the canopy temperature (Hall et al., 1991). As water evaporates, the surrounding air becomes gradually saturated and the evaporation rate slows down and eventually stops unless the saturated air is replaced by drier air. This replacement process depends greatly on wind speed. Hence, solar radiation, air temperature, air humidity and wind speed are climatological parameters to consider when assessing the evaporation process (Hall et al., 1991).

The evaporation component of the latent heat transfer (λE_e) can be approximated largely as a function of soil properties (Hillel, 1998) and surface roughness, but transpiration (λE_t) is more difficult to determine. To first order, λE_t can be considered proportional to the product of the air-canopy vapor pressure difference and the canopy conductance, a term that describes the bulk leaf stomatal conductance of water vapor from the canopy (Choudhury et al., 1986; Hall et al., 1991; Monteith, 1973).

$$\lambda E_t = \frac{\rho c_\rho \delta_e}{\gamma(r_c + r_a)} \tag{3}$$

where

γ	psychrometric constant (mbar^{0}K^{-1})
δ_e	vapor pressure deficit (mbar)
r_c	canopy resistance (s m^{-1}), defined as $1/g_c$, where g_c is canopy conductance
r_a	aerodynamic resistance for heat and water vapor (s m^{-1}).

Under temperate growing conditions, r_c is roughly an order of magnitude larger than r_a, and, as a result, the most significant drivers of λE_t are δ_e and g_s as defined in (2). δ_e is a well understood function of the relative humidity, the saturation vapor pressure at the evaporating surface and the saturation vapor pressure of the surrounding canopy air space, both of which are exponentially related to their respective temperatures. Several models exist to obtain δ_e; in this paper, we implemented an algorithm introduced by Monteith and Unsworth (1990). Remotely sensed estimates of photosynthesis were used to obtain g_s via the Ball–Berry–Collatz relationship (2), and scaled to g_c based on the assumptions of Sellers, Heiser, and Hall (1992), thus determining λE_t from remote sensing inputs.

2.2. Sensible heat transfer

Sensible and latent heat transfers can be modeled as simple, first-order solutions to the conservation equations for mass, momentum, and energy (Hall et al., 1991). Under the assumption that the boundary layer is horizontally homogeneous, and turbulent fluxes of heat and mass are only vertical, H is proportional to the difference

between the air temperature above the canopy and the temperature within the canopy air space (Hall et al., 1992; Sellers, Randall, et al., 1996).

$$H = \frac{\rho c_p (T_c - T_A)}{r_a} \quad (4)$$

where

ρ density of air (≈ 1.22521 kg m^{-3})
C_ρ specific heat of air ($\approx 1.006e-3$ J Kg^{-1} ^{0}K^{-1})
T_C canopy temperature (^{0}K^{-1})
T_A reference height air temperature (^{0}K^{-1}).

The aerodynamic resistance for heat and water vapor (r_a) characterizes the efficiency of the transfer of heat by turbulent air through the canopy into the air above, and is commonly derived using semi-empirical arguments to adjust the surface momentum transfer coefficient (Hall et al., 1991), a term that relates the vertical gradient in boundary layer wind speed to surface shear stress (Sellers, Randall, et al., 1996). A number of such empirical formulations exist for r_a; see for example Monteith (1973).

$$r_a = \frac{1}{u_m}\left(\frac{1}{k}\log\left(\frac{z_m - d}{z_0}\right)\right)^2 \quad (5)$$

where

u_m wind speed above the canopy (m s^{-1})
k von Kármán's constant (≈ 0.41)
z_m reference height (m)
z_0 roughness length (m)
d zero plane displacement (m).

z_0 relates to the height of terrain roughness elements and is used to model the wind speed deeper in the canopy and near the ground. It describes the theoretical height at which the wind speed becomes zero, when modeled as a log profile. Sellers, Randall, et al. (1996) calculate z_0 as an empirical function of canopy height (z_2) and leaf area (L),

$$z_0 = z_2\left(1 - 0.91e^{-0.0075L}\right) \quad (6)$$

Finally, the canopy surface temperature T_c can be determined from the emitted longwave radation $R_{L\uparrow}$ using the Stefan–Boltzmann law:

$$T_C = \left(\frac{R_{L\uparrow}}{\sigma \in}\right)^{\frac{1}{4}} \quad (7)$$

where σ is the Stefan–Boltzmann constant ($\approx 5.6704e-8$ Wm^{-2} 0K^{-1}) and $\in$ is the surface emissivity (gray body emissivity, here approximated using a factor of $\in = 0.99$) (Hall et al., 1992).

There are a number of challenges when using (4) to accurately infer sensible heat release, the more serious of which is the difference in the leaf temperature distribution in contact with the air that determines heat transport and the temperature of the leaves viewed by a thermal sensor (Hall et al., 1991). The temperature of leaves varies within the canopy and depends on wind speed and canopy architecture, thus the ensemble of leaves viewed by a sensor may not be representative of the leaves in contact with the atmosphere. Additionally, as can be seen in (7) kinetic temperature must be inferred from radiometric temperature, hence is exquisitely sensitive to variability in $\in$ that also can depend on sensor view angle. For these reasons, radiometric temperature viewed by a sensor can vary significantly in comparison to T_c causing sizable errors in the radiometric inference of H in (4). Nonetheless, when H is small compared to λE, as is often the case when photosynthesis is active, the contribution of the errors in H to the overall energy budget is small (Hall et al., 1991).

3. Data

3.1. Site description

Five research sites were selected to cover a variety of temperate and sub-arctic forest stands (Hall et al., 2012a; Hilker, Hall, Tucker, et al., 2012); including a coastal Douglas-fir (*Pseudotsuga menziesii* var *menziesii* (Mirb.)) dominated stand on Vancouver Island (DF49), an Aspen (*Populus tremuloides* Michx.) dominated forest in Central Saskatchewan (SOA) and three Mountain Pine beetle (*Dendroctonus ponderosae* Hopk.) affected lodgepole pine (*Pinus contorta* Dougl. ex. Loud var. *latifolia* Engl.) stands in Northern British Columbia (Fig. 1). Table 1 contains an overview, references and site description for each individual stand and the dates the spectral and flux data were acquired. The three beetle infested sites were selected to observe the potential of obtaining carbon fluxes from remote sensing across stands with similar species and structural conditions yet undergoing a major disturbance. The Kennedy siding site was initially infested by mountain pine beetle in August 2006. The canopy was still largely green in late April of 2007 with most of the attacked trees turning red during late May through early June and the health status of the canopy continuing to decline through to October. Data at the Summit Lake and Crooked River site were collected after the infestation took place; while Summit Lake was salvage logged, the Crooked River site was left untouched. Further information can be found in Hilker, Hall, Black, et al. (2012).

3.2. Eddy covariance measurements

Eddy covariance measurements of carbon and heat fluxes were acquired as part of the Canadian Carbon Program (Margolis, Flanagan, & Amiro 2006). At DF49 and SOA, carbon fluxes were measured using a three-axis sonic anemometer–thermometer (Model R3, Gill Instruments Ltd., Lymington, UK) and a closed-path CO_2/H_2O infrared gas analyzer (IRGA) (LI-6262 or LI-7000, LI-COR Inc., Lincoln, NE, USA) (Barr et al., 2004;Jassal et al., 2007). At the Northern BC sites, a three-axis sonic anemometer–thermometer (Model CSAT3, Campbell Scientific Inc., Logan UT, USA) and an open-path CO_2/H_2O IRGA (Model LI-7500, LI-COR Inc.) were used (Brown et al., 2010). Latent and sensible heat fluxes were determined using measures of air temperature and relative humidity measured at each of the sites.

Net radiation was determined using a four-way net radiometer, except for the Kennedy siding site, where R_N was computed using the difference between up and downward looking long and shortwave radiation

$$R_N = \left(R_{S\downarrow} + R_{L\downarrow}\right) - \left(R_{S\uparrow} + R_{L\uparrow}\right) \quad (8)$$

where $R_{S\downarrow}$, $R_{L\downarrow}$, $R_{S\uparrow}$, $R_{L\uparrow}$ are down and upwelling short and longwave radiation measurements, respectively.

Soil heat flux measurements were available from soil heat flux plates at all sites except for SOA. Rate of change in CO_2 storage in the air column was calculated from the half-hour average CO_2 concentrations obtained at EC measurement height (Morgenstern et al., 2004).

3.3. Stand level remote sensing

Stand level canopy spectra were acquired from an automated, multi-angular spectroradiometer, Amspec I (Hilker et al., 2007) and Amspec II (Hilker, Nesic, Coops & Lessard, 2010), mounted on top the flux towers at each site between 2006 and 2010 (Fig. 2, Table 1). Amspec II features a

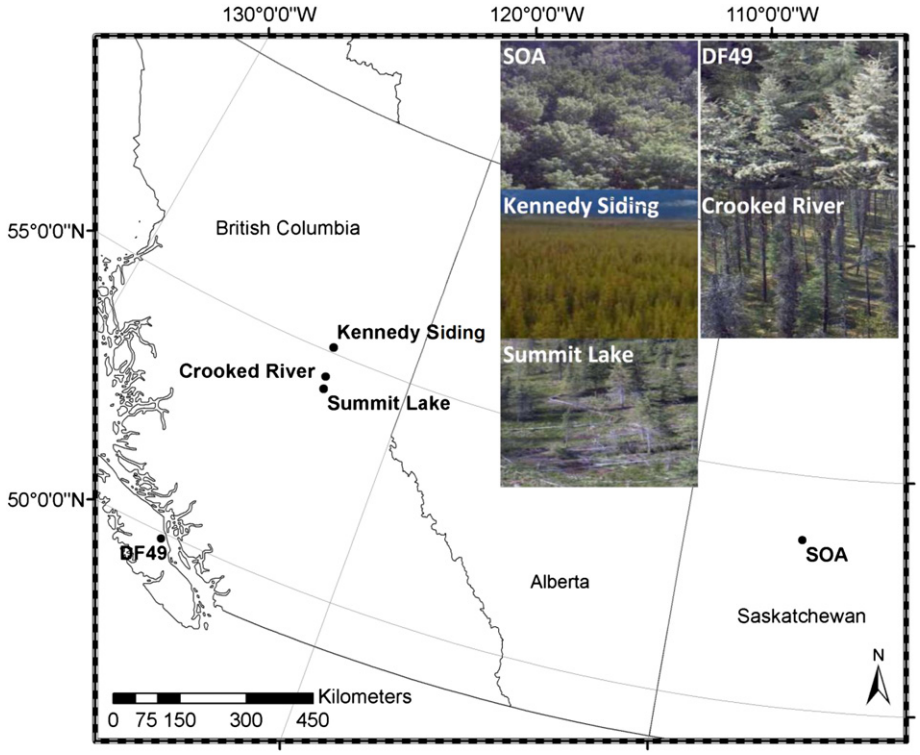

Fig. 1. Tower locations and site overview. The inset shows in situ photographs of each of the sites to illustrate their canopy structure.

pan-tilt unit which allows the sensor head to be oriented at any view zenith angle between 43° and 78° and azimuth between 0 and 360°. Measurements before 2009 were made using the prototype version, Amspec I (Hilker et al., 2007), operating at a fixed vertical zenith angle of 62° (Chen & Black, 1992). To allow sampling under varying sky conditions, canopy spectra were obtained from simultaneous measurements of solar irradiance and radiance, sampled continuously from sunrise to sunset at a 5° angular step width (horizontally and vertically), with the full rotation completed every 15 min. The spectroradiometer used is a Unispec-DC (PP Systems, Amesbury, MA, USA) featuring 256 contiguous bands with a nominal band spacing of 3 nm and a nominal range of operation between 350 and 1200 nm. The reflectance at 531 and 570 nm was used to derive PRI at an hourly basis (Hilker et al., 2008). Corresponding canopy shadow fractions were then calculated using a hillshade algorithm based on LiDAR. The technique has been presented in detail in previous work (Hilker, Nesic, Coops & Lessard, 2010).

3.4. CHRIS/Proba imagery

Satellite observations were acquired from the Compact High Resolution Imaging Spectroradiometer (CHRIS) on board the European Space Agency's Platform for Onboard Autonomy (Proba). CHRIS is an imaging spectrometer with a 615 km sun-synchronous orbit and an orbital repeat cycle of approximately 7 days. Its maximum spatial resolution is 18 m or 34 m at nadir, depending on the mode setting, with a swath width of 14 km. The CHRIS/Proba configuration permits along-track narrow-band spectrometric observations of up to five angles (+55°, +36°, 0°, −36°, −55°). This data is acquired nearly simultaneously within each overpass during which stand level ε may be considered constant. Satellite observations of top of atmosphere (TOA) radiance were converted to reflectance (Gomez-Chova et al., 2008) and screened for clouds (Thuillier et al., 2003). A two step geo-rectification algorithm was applied (Ma et al., 2010) and CHRIS/Proba satellite images were co-registered to a Landsat scene of the same location (Hilker et al., 2011). No suitable atmospheric correction algorithm currently exists for multi-angular observations, as the commonly used assumption of a Lambertian reflectance is not true for PRI due to the complex interaction of changing ε under variable radiation conditions (Hilker, Lyapustin, et al., 2009). As a result, TOA reflectance was used in this analysis with impacts calculated and described in Hall et al. (2011). PRI was computed from CHRIS/Proba imagery as the normalized difference of CHRIS bands 4 (529 nm, Bandwidth: 12.9 nm) and 6 (569 nm,

Table 1
Study site descriptions and acquisition dates.

Site, reference	Lat (°)/long (°)	Elev (m)	Dominant species	LAI	Age (yrs)	Height (m)	Annual mean temp. (°C)	Data acquisition dates
Campbell River (DF49) (Morgenstern et al., 2004)	−125.334 49.867	340	*Pseudotsuga menziesii*, *Thuja plicata*, *Tsuga heterophylla*	7.1	60	35	8.1	2006/04/01–2007/03/31
Kennedy Siding (MPB-06) (Brown et al., 2010; Hilker, Coops, et al., 2009)	−122.840 55.112	750	*Pinus contorta*, *Abies lasiocarpa*, *Picea glauca* Understory: *Alnus tenuifolia*, *Salix* spp., *Vaccinium* spp.	1.3	80	15	≈2.3	2007/04/25–2004/10/18
Crooked River (MPB-03) (Brown et al., 2010)	−122.713 54.473	710	*Pinus contorta*, *Abies lasiocarpa*, *Picea glauca* Understory: *Salix* spp., *Vaccinium* spp.	0.9	110	17	≈2.3	2010/07/10–2010/08/24
Summit Lake (MPB-09)	−122.614 54.224	800	*Pinus contorta*	0.5	110	17	≈2.3	2010/07/10–2010/08/24
Southern Old Aspen (SOA) (Barr et al., 2004)	106.198−52.629	600	*Populus tremuloides*, Understory: *Corylus cornuta*	2.1	83	22	0.4	2009/05/26–2009/11/04

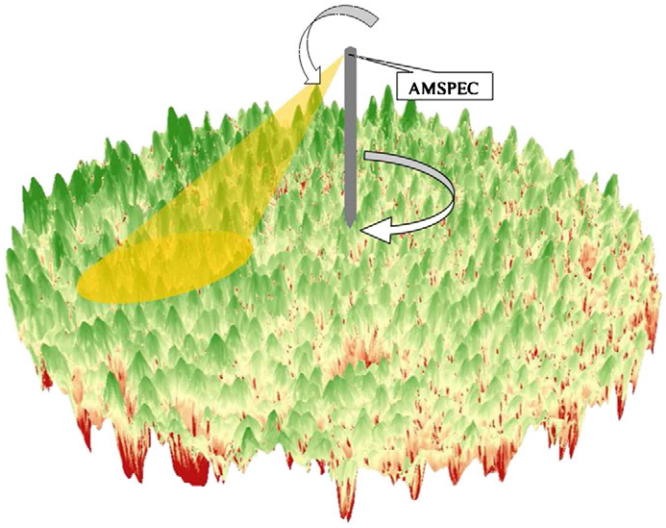

Fig. 2. Illustration of a stand level AMSPEC system. The instrument features a pan-tilt unit which allows the sensor head to be moved at any zenith angle between 40 and 78° at a view azimuth between 0 and 360°. The upward looking sensor features a cosine diffuser to correct for varying solar altitudes. Canopy reflectance is determined from solar irradiance and canopy radiance. A webcam picture is automatically taken with every spectrum that is sampled (Hall et al., 2008).

Bandwidth: 14.1 nm). Canopy shadow fractions were derived for each pixel of each observation using spectral mixture decomposition based on the sequential maximum angle convex cone (SMACC) model (see Hilker et al., 2011 for details).

3.5. Computing ε from multi-angle PRI

The theoretical and practical steps for computation of ε and GPP from multi-angle remote sensing data have been discussed and validated in detail elsewhere (Hall et al., 2011, 2008; Hilker, Hall, Black, et al., 2012; Hilker, Hall, et al., 2010) and are only briefly summarized here to aid with the understanding of its use as input to the stomatal conductance model. Photosynthetic light use efficiency is a direct function of the amount of solar irradiance on a given leaf and for a given level of resources available to support the photochemical reaction process (Demmig-Adams & Adams, 1996). In cases where photosynthesis is limited by factors other than light ($\varepsilon < \varepsilon_{opt}$), ε is closely related to canopy shadow fraction (α_s) as sunlit leaves are more likely to be exposed to excess radiation levels than shaded leaves (Hall et al., 2008). This relationship however, disappears under conditions where light is limiting GPP ($\varepsilon = \varepsilon_{opt}$), as in this case, photosynthesis is no longer light limited and will, by definition, not be down-regulated in either sunlit or shaded leaves (Hilker et al., 2011). This concept has two important implications for remote sensing of ε using PRI. First, stand level ε cannot be inferred from traditional, mono-angle PRI observations, because the proportion of α_s observed by the sensor at a given time may not be representative of the canopy and the contribution of α_s to the photosynthetic down-regulation is unknown. For instance, the relationship of PRI to ε can change by 100% over the range of shadow fractions (Hall et al., 2011) and is also dependent on the unstressed PRI of the photosynthetic and PRI of the non-photosynthetic materials and background. Second, multi-angular measurements of PRI can be used as a generic measure of stand-level ε, if α_s is known for each view angle. We have shown in previous research that this second hypothesis is true, because under the assumption of singular leaf scattering, which is reasonable for remote sensing of wavelengths in the visible bands, a normalized difference reflectance index does not change its value with the viewing geometry unless the value of one of its bands changes as a physiological response of the degree of leaf illumination (Hall et al., 2008). Based on these two principles it can be concluded that the first derivative of PRI with respect to shadow fractions (PRI′) can be used to infer instantaneous ε at the canopy level as long as as the time interval between these multi-angle observations is short, and the physiological conditions can be considered constant. In previous work, we have used both AMSPEC (Hilker, Hall, et al., 2010) and CHRIS/Proba (Hilker et al., 2011) across multiple sites and compared these measurements to eddy covariance derived estimates of NEP, GPP and respiration(Hall et al., 2012a; Hilker, Hall, Black, et al., 2012; Hilker, Hall, Tucker, et al., 2012b) (Fig. 3).

4. Results

To first order, sensible heat fluxes were driven by temperature differences between the surface and the surrounding air column. Fig. 4 shows the range of air (T_A) and canopy temperatures (T_C), estimated from upwelling thermal radiation, for all five AMSPEC sites (Eq. (6)). For reasons of clarity, data from SOA, DF-49 and Kennedy Siding are presented as weekly averages; for Crooked River and Summit Lake, only two months of observations were available, and consequently, these data are presented as daily averages (Figure D and E). Air and canopy temperatures ranged between −5 and +30 °C during the observation period across all sites. Largest seasonal differences were found at the SOA site, which was exposed to the most continental climate, whereas seasonal changes were smallest at the costal DF-49 site. T_C followed T_A closely across all sites. Differences between T_C and T_A were larger during the summer, with average T_C being typically higher than T_A, while T_C was mostly equal to or lower than T_A during spring and fall season. While differences between T_C and T_A were small (around 0.5 °C) at SOA and DF49, much larger differences were found at the three Mountain Pine affected sites, in particular Crooked River. This is likely because there is no closed canopy at this site and the radiometer is viewing the warm background and tree limbs (at a view zenith of 63°).

Fig. 5 shows a comparison of hourly H observed from the eddy covariance system and modeled as a function of T_A, T_C and r_a. Across all sites, the simple model shown in Eq. (3) predicted *H* fluxes reasonably well, the coefficients of determination ranged between $r^2 = 0.42$ (Kennedy siding) and $r^2 = 0.76$ (DF49) ($p < 0.05$). In addition, the modeled H fluxes followed the 1:1 line closely, and little to no bias was found between modeled and measured heat fluxes.

The seasonal variation of the main drivers of λ*E* as modeled in Eq. (7) is shown in Fig. 6. A to C represent weekly averages, for D and E, daily mean values are provided. For wind speed (V), T_A and D, only the arithmetic means are shown, GPP values derived from AMSPEC are presented as mean and standard deviations. SOA, DF49

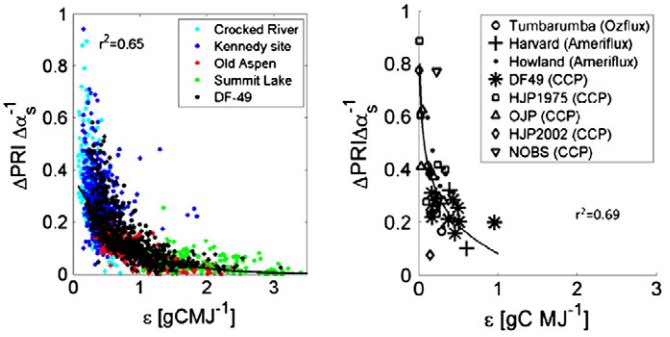

Fig. 3. Relationship between PRI′ and EC measured ε across structurally and physiologically very diverse study sites in Canada. The figure demonstrates the consistency of our method across scales. The left column shows tower based observations, the right side shows satellite based observations using CHRIS/Proba. Figure adapted from (Hilker, Hall, Black, et al., 2012; Hilker et al., 2011), see these publications for more information.

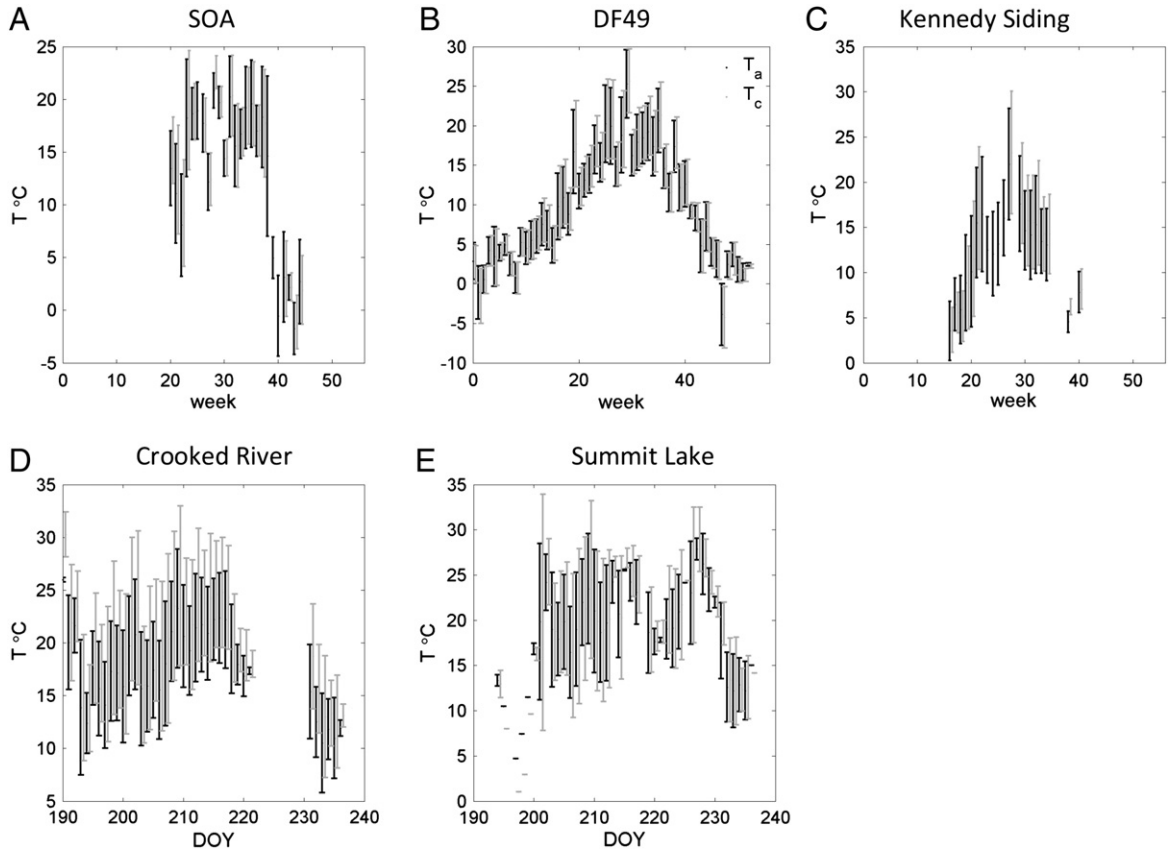

Fig. 4. Air (T_A, black) and canopy temperature (T_C, gray) for the observation period across the five tower sites. Data in A–C are presented as weekly averages; for Crooked River and Summit lake daily averages are presented as only two months of observations were available for these sites. The error bars show the standard deviation around the mean values.

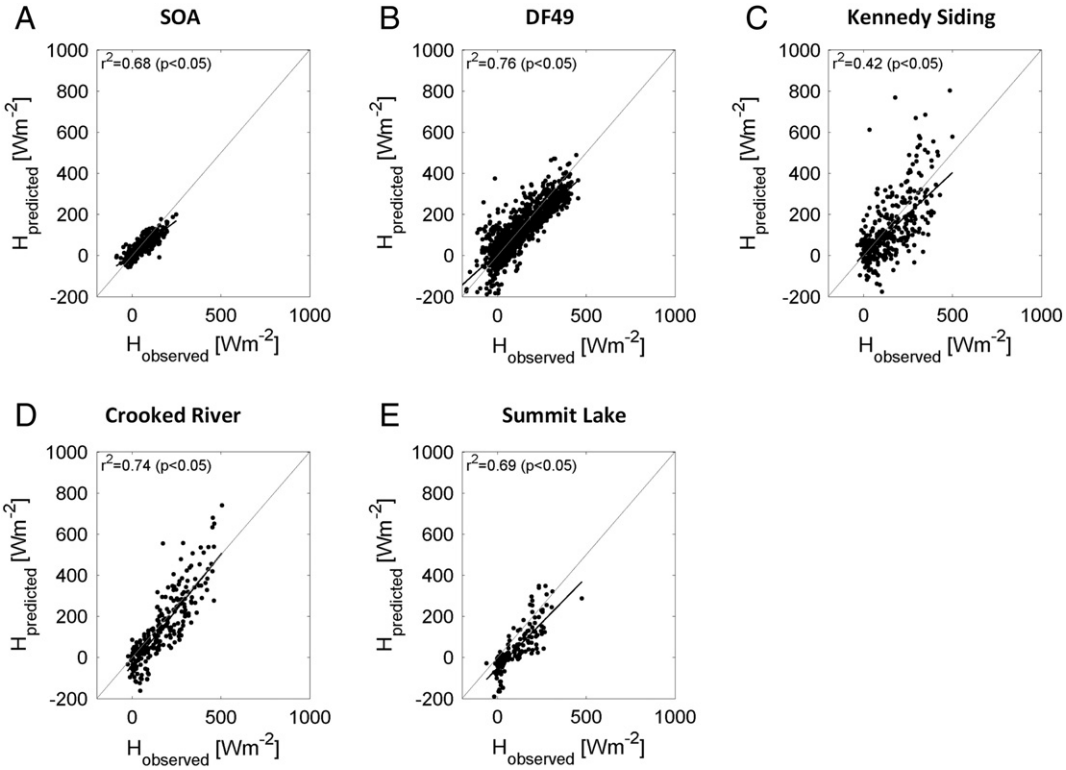

Fig. 5. Comparison between measured and modeled fluxes of *H* for the five different tower sites. The gray line represents the 1:1 relationship, the black line is the linear regression between observed and predicted values. Data are shown as hourly averages, only daytime observations are presented.

and Kennedy siding illustrated distinct seasonal patterns throughout the observation period. Estimates of V, T_A, GPP and D were highest during the summer and smallest at the beginning and end of the growing season. AMSPEC estimated productivity was highest at the DF49 site with extremes of up to 40 μmol m^{-2} s^{-1} and weekly means of around 25 μmol m^{-2} s^{-1}. Productivity at SOA stayed high during the summer but showed a steep decline towards the end of the growing season. All three Mountain Pine beetle affected sites showed little productivity during the observation period, with only around 5 μmol m^{-2} s^{-1} on average. Consistent with these findings, D was notably higher at the disturbed sites, especially at the partially harvested, salvage logged, Summit Lake site.

Fig. 7 shows a comparison between modeled λE_t and measured λE for all five tower sites. The coefficients of determination between observed and predicted λE and λE_t fluxes ranged between $r^2 = 0.16$ for the Kennedy Siding Site and $r^2 = 0.78$ for the SOA site ($p < 0.05$). Note that the EC-system measures total λE whereas the modeled fluxes obtained from AMSPEC account only for λE_t, that is our model does not consider heat fluxes originating from evaporation of water from soil and open surfaces. The magnitude of the soil evaporation itself was not measured, however, to first order a qualitative assessment can be made when comparing fluxes to soil temperatures, which is indicative of soil evaporation. In Fig. 7, soil temperatures (T_{Soil}) are color coded, with blue markers representing colder, moister soils and red dots representing warmer, drier soils. The loamier soil type found at DF49 resulted in larger deviations of observed and predicted λE fluxes, whereas the sandier soil types yielded a better correspondence between measured and predicted λE fluxes (Fig. 7A and B). The relative contribution of λE_t to total λE fluxes is also expected to depend on the density of vegetation. As a result, the performance of the model presented in Fig. 7 can be related to green leaf area, as approximated for instance using NDVI. Fig. 8 shows the relationship between AMSPEC measured NDVI (BRDF normalized data from early August shown) and the coefficients of determination of the 5 study sites presented in Fig. 7.

Latent and sensible heat fluxes were inversely related to r_a and r_c. Fig. 9a shows the seasonal variation of r_a, r_c, H and λE_t for the DF49 site. The aerodynamic resistance was highest during the winter months with little to no difference found between T_C and T_A, but dropped considerably during the vegetation period. The latent heat flux was largely dominated by evaporation (E) outside the vegetation season, but was mostly driven by transpiration (T) during the summer months (Fig. 9b). Here, E is computed as $\lambda E_e = \lambda E - \lambda E_t$ and converted to units of grams of water m^{-2} s^{-1}; the figure represents daily averages. Fig. 9c illustrates a comparison between evapotranspiration (ET), T and E directly after a rain event. The figure shows averaged data for 6 rain events during the summer of 2006 for which there was no additional rain for at least 10 days before and at least 10 days after the event. Directly after the rain, E is high due to evaporation of water from wet surfaces, but decreases steadily as the surface dries up. Transpiration is low first, but increases as more water is transported to the root zone and into the leaves. As would be expected, E was highly correlated to measures soil moisture, after applying a lag of 8 days (see Fig. 9c) to minimize the effect of free surface water evaporation (Fig. 9d). High soil moisture was associated with high heat flux from the atmosphere into the soil (blue dots), whereas dry soils where associated with inversed heat fluxes from the soil back into the atmosphere.

Fig. 10 illustrates a comparison between the energy balances obtained from net radiation and soil heat flux measurements and the balance modeled using remotely sensed inputs. In all cases strong, linear relationships were found between modeled and observed fluxes with coefficients of determination ranging between $r^2 = 0.64$ and $r^2 = 0.85$. Predictions were best for the undisturbed sites, but accurate estimates of the energy balance were also possible in case of the disturbed sites. Note that no soil heat flux measurements were available at SOA; this limitation is acknowledged, the error, however, is expected to be small, as the vast majority of the energy flux at this site should originate from R_N. The mean and standard deviation of the diurnal variability of the evaporative fraction (EF), defined as $\lambda E\, R_N^{-1}$

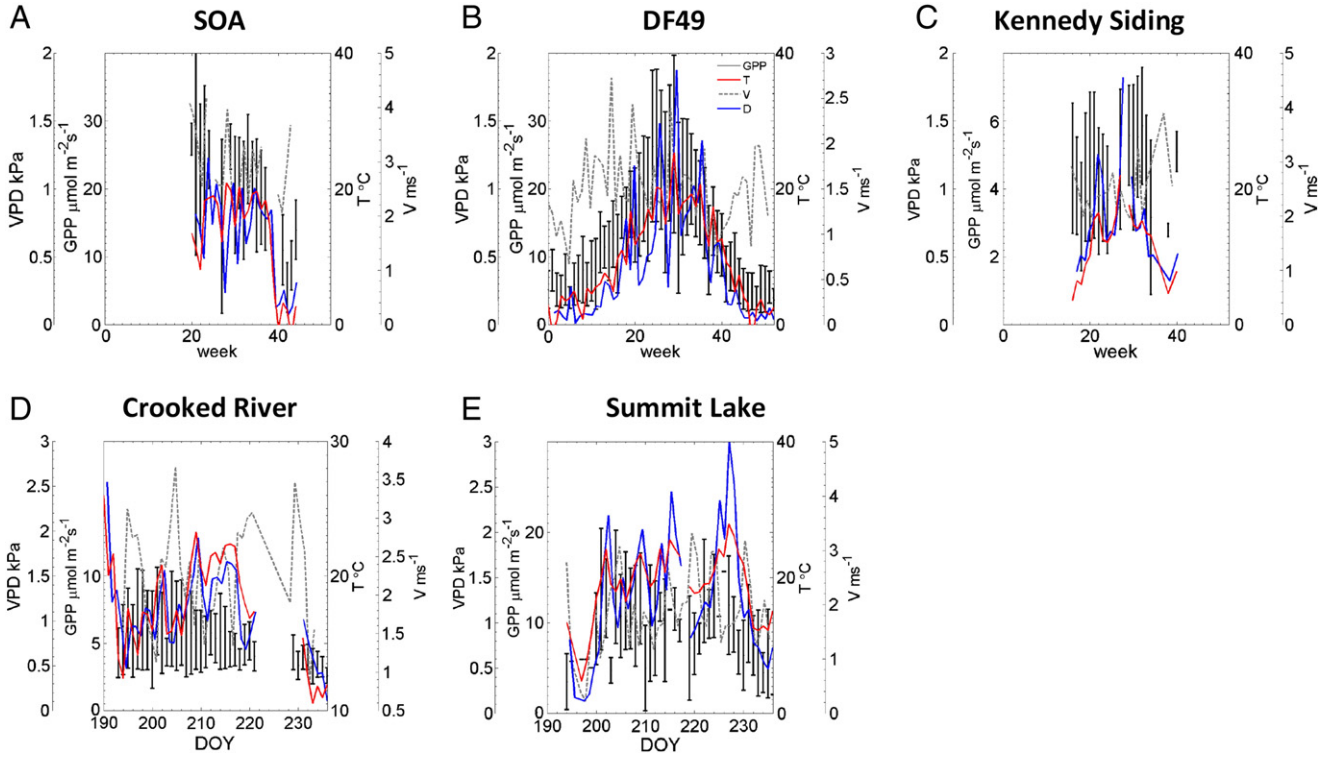

Fig. 6. Seasonal variability of GPP, air temperature (T), wind speed (V) and atmospheric vapor pressure deficit (D) across all sites. Again, A–C represent weekly averages, for D and E, daily means are shown. The error bars represent mean and standard deviation of GPP estimated from AMSPEC.

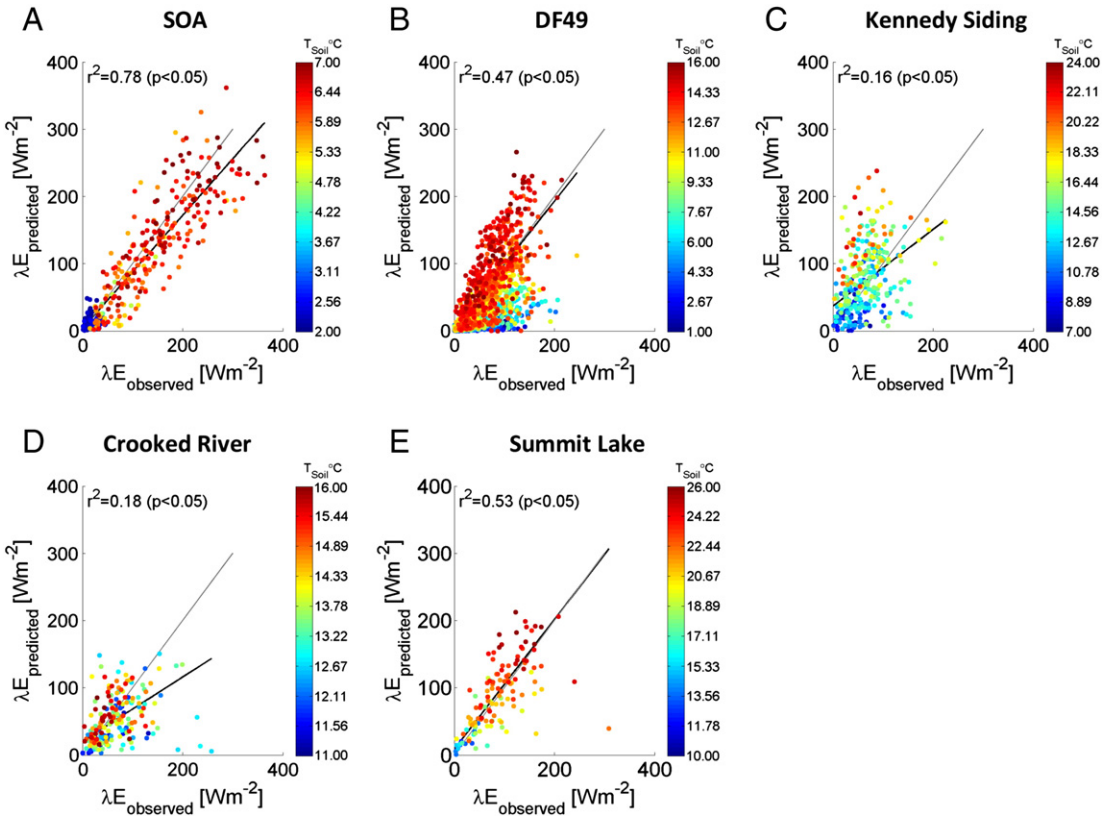

Fig. 7. Comparison between measured (x-axis) and modeled (y-axis) λ*E* fluxes across the five different tower sites. The color code of the observations corresponds to the soil temperature as indicated by the color bar next to the figure. The gray line represents the 1:1 relationship, the black line is the linear regression between observed and predicted values. Data are shown as hourly averages, only daytime observations are presented. Slope factors for the different biome types required in Eq. (2) were obtained from Sellers, Randall, et al. (1996).

is presented in Fig. 11. For reason of comparability, and to avoid the impact of seasonal effects, only data for July and August are shown in this example. Note that the solar azimuth angle was used instead of local time to allow a more objective comparison between sites. While EF was relatively small and changed little during the day, a much larger variability was found in the early morning and late afternoon hours, closer to sunrise and sunset.

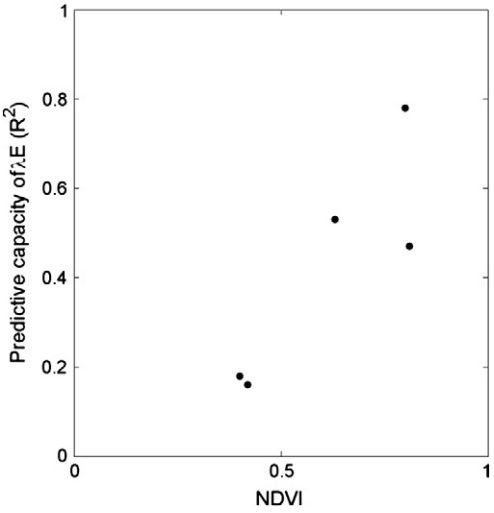

Fig. 8. Dependence of the performance of using λE_t for predicting λ*E* fluxes (Fig. 7) on green vegetation density, here approximated using NDVI (we used BRDF normalized AMSPEC data acquired during early August). The contribution of transpiration to total λ*E* is expected to be relatively larger at densely vegetated site and relatively smaller at sparsely vegetated or disturbed sites.

Fig. 12 demonstrates fluxes of λ*E* derived from multi-angle satellite observations of GPP, during two CHRIS/Proba overpasses. The figure clearly illustrates the dependency of λ*E* on canopy structure, but also meteorological and physiological drivers. During the overpass observed in June 2009, growing conditions were less favorable due to water shortage reflected in relatively low humidity, and high incident PAR (1543 Wm^{-2}) resulted in relative closure of the stomata. As a result, ε was low during this time (0.4 g C MJ^{-1}) and λ*E* did not exceed 200 Wm^{-2}, only around 10% of the total energy balance on that day. During the second overpass on September 17, growing conditions were more favorable, with less incident PAR and relative humidity of close to 90%. The high ε value of 1.6 g C MJ^{-1} suggests that stomata must have been widely opened during this time. As a result, almost 60% of the incoming solar energy was balanced as λ*E* flux.

5. Discussion

In summary, the study presented in here has demonstrated that remote sensing of *H* and λ*E* is possible at the stand level. It is important to note that when scaling these measurements to space, additional operational issues (availability of satellite coverage) and technical issues (atmospheric correction, sensor design) will need to be addressed. Nonetheless, we have shown that all components of surface energy balance can be quantified from either remote sensing or climatological inputs. As a result, this work may serve as a first step towards using satellite based acquisitions for quantifying the surface energy balance globally.

The radiation based temperature gradient between canopy surface and surrounding air column (Fig. 4) together with estimates of the aerodynamic resistance based on wind speed and canopy roughness (Sellers, Randall, et al., 1996) explained between 68% and 76% of the

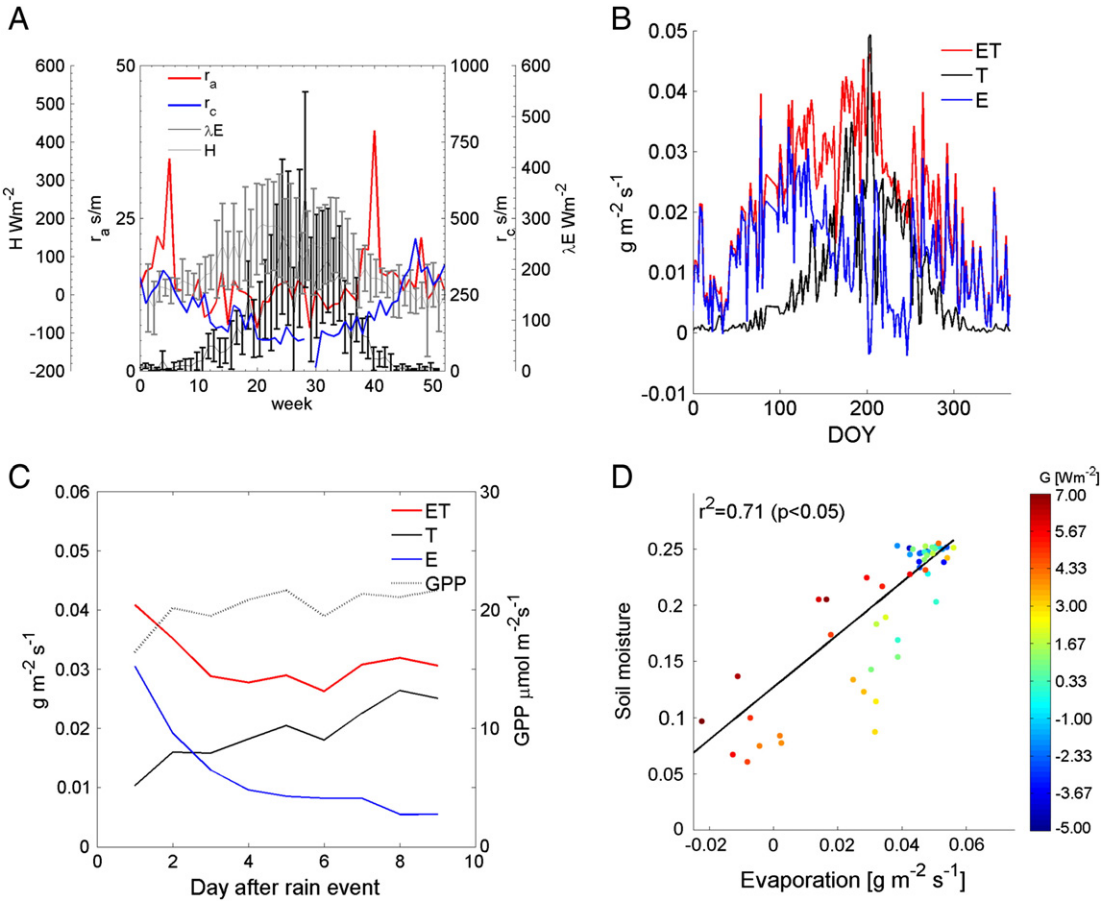

Fig. 9. (A) Seasonal variability of H, λE, r_a and r_c for the example of the DF49 site. The error bars represent the standard deviation of H and λE, respectively. (B) Seasonal variability in λE_e–λE_t and evaporation for the example of the DF49 site. (C) Changes ET, T and E for 10 days following a rain event averaged over 6 precipitation events in the summer of 2006. (D) Weekly relationship between soil evaporation ($E = \lambda E_e - \lambda E_t$) and soil moisture. To minimize the effect from free surface water evaporation an 8 day lag is applied. The color code corresponds to the soil heat flux as indicated in the color bar.

tower inferred sensible heat fluxes across all sites, with the exception of the Kennedy Siding site, where the coefficient of determination was notably lower ($r^2 = 0.42$, $p < 0.05$). A likely explanation for the results at this site is a change in canopy roughness and canopy closure during the observation period, as the stand condition deteriorated rapidly due to the ongoing Mountain Pine beetle attack, which killed more than half of the existing trees (Brown et al., 2010; Hilker, Coops, et al., 2009). Our algorithm did not account for this decline due to a lack of repeated measurements of green leaf area (Eq. (6)). Despite the differences in structure and phenology, modeled H fluxes were not biased when compared to EC-measured H, which confirms the potential for a broader application of this model at least across temperate and sub-arctic forest sites (Choudhury et al., 1986; Sellers, Los, et al., 1996). Previous research has shown that canopy temperature is sensitive to the surface emissivity ($\in$)(Hall et al., 1991). For most canopy types, the emissivity can be approximated using a value of close to 1 (Hall et al., 1991) as photosynthetic material is highly absorptive in the visible wavebands. The constant assumed in this study worked well across the examined sites; in cases where this assumption does not hold, $\in$ could be inferred from model inversion where the energy balance of the surface is known (such as flux tower sites). The H calculation assumes the skin temperature determined by outgoing longwave radiation matches the aerodynamic temperature.

Latent heat fluxes from canopy transpiration quantified by remote sensing inputs were strongly related to those observed from EC measurements. While λE_t comprises most of λE in forested ecosystems (Collatz et al., 1991), λE of grasslands or sparsely vegetated surfaces is less dominated by water uptake through plants (Fig. 8). The contribution of λE_e is expected to vary with soil type (Fig. 7A and B), vegetation density (as demonstrated in Fig. 8), and the quantities and timing of precipitation events (Crago & Brutsaert, 1996). Further research will be needed to assess these differences across different ecosystems. The combination of eddy flux obtained λE fluxes and remote sensed λE_t may, however, provide new opportunities for estimating the contribution of soil and surface water evaporation in vegetated ecosystems. Contributions of E and T to overall ET shown in Fig. 9c can be confirmed by previous findings (Hall et al., 1991; Sellers et al., 1997) and may have important implications for meteorological and ecological applications.

Our model based on remote sensing inputs accurately predicted surface heat fluxes across all sites (as obtained from R_N–G), and modeled values were within 10% of the micrometeorological observations (Fig. 10). This is an important result, as it demonstrates the capacity of remote sensing driven algorithms to scale tower based measurements of the surface energy balance using GPP, net radiation, wind speed, humidity and temperature. At the tower level, our method also serves as an independent validation of previously derived spectral estimates of daytime GPP at the stand level (Hilker, Hall, Black, et al., 2012) and highlights the potential of multi-angular data for remote sensing of terrestrial carbon fluxes. Trends and results shown for the evaporative fraction (EF) of heat fluxes across all sites (Fig. 11) agree well with findings of previous work, which showed little variation of this fraction during daytime but larger variability at low solar zenith angles and during night time (Sugita & Brutsaert, 1991). Reasons for the stability of EF during daytime hours include its dependence on the available energy and

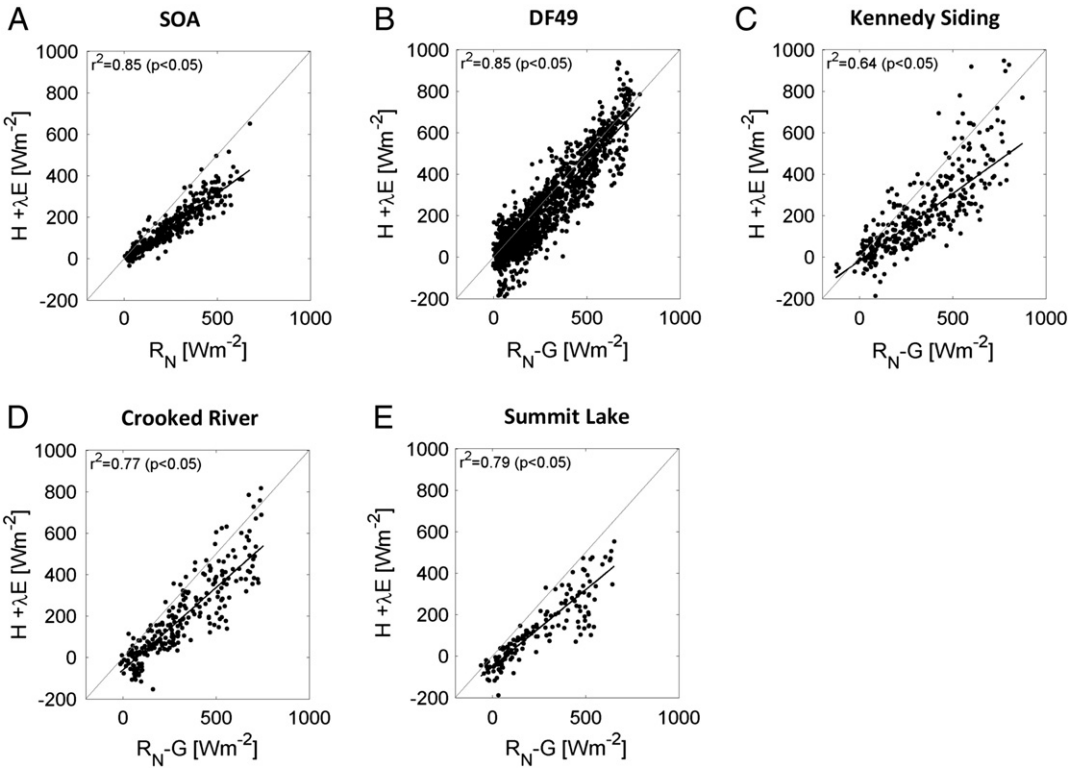

Fig. 10. Assessment of the energy balance across the five different tower sites. The axis represents the net heat fluxes obtained from R_N–G, the y-axis shows the sum of λE *and* H obtained in this study. The gray line represents the 1:1 relationship, the black line is the linear regression between observed and predicted values. Data are presented as daytime, hourly observations.

daytime progressions the humidity, temperature, and surface resistance (Crago & Brutsaert, 1996). Our approach assumes that the Ball–Berry equation (and the original m and b coefficients) holds across a range of stress levels associated with changes in PRI. Further research may be required to confirm the linearity of this relationship across different vegetation types.

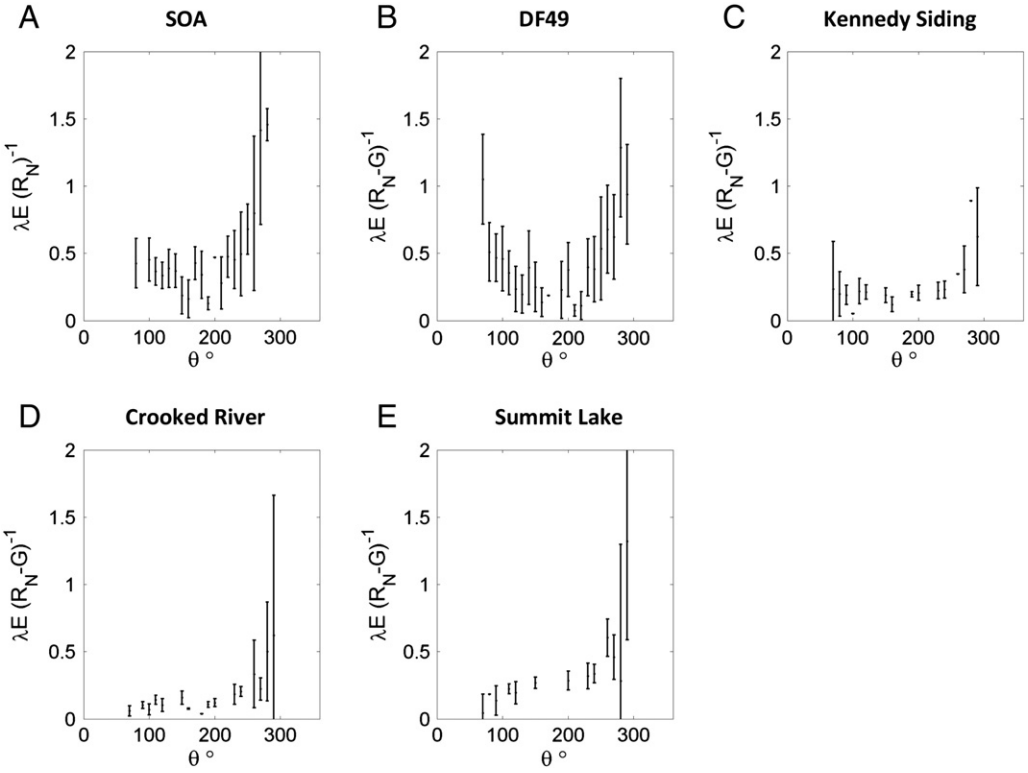

Fig. 11. Evaporative fraction across the five different tower sites shown as function of the solar azimuth angle (θ) and observed during the months of July and August. The error bars represent the standard deviations around the mean values.

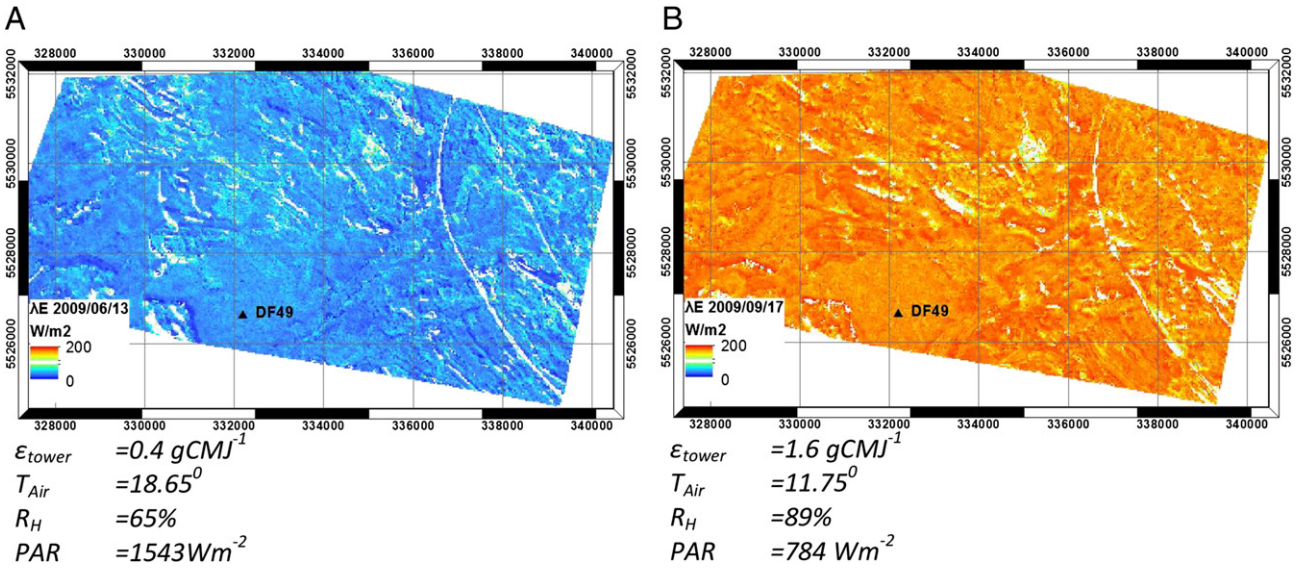

Fig. 12. CHRIS Proba derived demonstration of λ*E* based on satellite derived estimates of ε and GPP (Hilker, Hall, Tucker, et al., 2012b) and tower-measured meteorological observations. A represents a case where λ*E* was relatively low (June 13, 2009), B shows scene during an overpass where λ*E* was relatively high (September 17, 2009) the status of some of the most important meteorological and physiological drivers is listed below the figures.

While eddy covariance systems are essential for measuring and understanding the temporal variability in carbon and energy fluxes, remotely sensed inputs can help us to understand the variability of these fluxes spatially. This information may be combined with temporally continuous measures of meteorological data to obtain more realistic estimates of carbon and energy fluxes globally. The results in Fig. 12 are intended as a demonstration of how spaceborne acquisitions of λE_t depend on canopy structure as GPP is highly dependent on canopy shading (Hilker et al., 2008). It is acknowledged that more sophisticated techniques and validation will be needed to account for spatial heterogeneity of temperature, humidity and wind speed (all of which require appropriate inputs from remote sensing). Global meteorological datasets are available for instance through Scripps Oceanographic Institute (Piper, 1995) or NASA's Distributed Information Services for Climate and Ocean Products and Visualizations for Earth Research (DISCOVER). While CHRIS/Proba allows us to obtain multi-angle assessment of PRI, the current limitations of this sensor are also acknowledged (Hilker et al., 2011). The results presented in Fig. 12 should therefore be seen only as a demonstration of the potential of multi-angular satellite data for the exploration of the vegetation carbon and energy cycle. The acquisition of spatially-contiguous, high temporal frequency measurements of ε and GPP will require a completely new mission design, such as proposed in Hall et al. (2011).

While CHRIS/Proba cannot be used in an operational sense, this satellite platform does, provide a unique opportunity to further test and develop the use of multi-angular spaceborne data for acquiring information about the terrestrial carbon and energy budget. One focus of new research should therefore be to use these existing data for specification of system design and science requirements for a new space borne mission designed to address these challenges and advance our understanding of the impact of terrestrial vegetation on our climate.

Acknowledgments

Thank you to Zoran Nesic, Dominic Lessard, Andrew Hum and Rick Ketler from UBC Faculty of Land and Food Systems (LFS) for their assistance in technical design, installation, and maintenance of Amspec and Amspec II. Mathew Brown is thanked for analyzing the EC data. The quality control for the climate data at SOA was done by Alan Barr. This research was partially funded by the Canadian Carbon Program (Canadian Foundation for Climate and Atmospheric Science (CFCAS), the Natural Sciences and Engineering Research Council of Canada (NSERC) and BIOCAP, and an NSERC-Accelerator grant to Coops.

References

Anderson, M. C., Norman, J. M., Kustas, W. P., Houborg, R., Starks, P. J., & Agam, N. (2008). A thermal-based remote sensing technique for routine mapping of land-surface carbon, water and energy fluxes from field to regional scales. *Remote Sensing of Environment*, *112*, 4227–4241.

Aubinet, M., Grelle, A., Ibrom, A., Rannik, U., Moncrieff, J., Foken, T., et al. (2000). Estimates of the annual net carbon and water exchange of forests: The EUROFLUX methodology. *Advances in Ecological Research*, *30*(30), 113–175.

Baldocchi, D. D., & Wilson, K. B. (2001). Modeling CO_2 and water vapor exchange of a temperate broadleaved forest across hourly to decadal time scales. *Ecological Modelling*, *142*, 155–184.

Ball, J. T. (1988). *An analysis of stomatal conductance*. Stanford, CA: Stanford University, 89.

Barr, A. G., Black, T. A., Hogg, E. H., Kljun, N., Morgenstern, K., & Nesic, Z. (2004). Inter-annual variability in the leaf area index of a boreal aspen–hazelnut forest in relation to net ecosystem production. *Agricultural and Forest Meteorology*, *126*, 237–255.

Bastiaanssen, W. G. M., Menenti, M., Feddes, R. A., & Holtslag, A. A. M. (1998). A remote sensing surface energy balance algorithm for land (SEBAL) — 1. *Formulation. Journal of Hydrology*, *213*, 198–212.

Bastiaanssen, W. G. M., Pelgrum, H., Wang, J., Ma, Y., Moreno, J. F., Roerink, G. J., et al. (1998). A remote sensing surface energy balance algorithm for land (SEBAL) — 2. *Validation. Journal of Hydrology*, *213*, 213–229.

Brown, M., Black, T. A., Nesic, Z., Foord, V. N., Spittlehouse, D. L., Fredeen, A. L., et al. (2010). Impact of mountain pine beetle on the net ecosystem production of lodgepole pine stands in British Columbia. *Agricultural and Forest Meteorology*, *150*, 254–264.

Chen, J., & Black, T. (1992). Foliage area and architecture of plant canopies from sunfleck size distribution. *Agricultural and Forest Meteorology*, *60*, 249–266.

Choudhury, B. J., Reginato, R. J., & Idso, S. B. (1986). An analysis of infrared temperature observations over wheat and calculation of latent-heat flux. *Agricultural and Forest Meteorology*, *37*, 75–88.

Collatz, G. J., Berry, J. A., Farquhar, G. D., & Pierce, J. (1990). The relationship between the Rubisco reaction-mechanism and models of photosynthesis. *Plant Cell and Environment*, *13*, 219–225.

Collatz, G. J., Ball, J. T., Grivet, C., & Berry, J. A. (1991). Physiological and environmental-regulation of stomatal conductance, photosynthesis and transpiration — A model that includes a laminar boundary-layer. *Agricultural and Forest Meteorology*, *54*, 107–136.

Crago, R., & Brutsaert, W. (1996). Daytime evaporation and the self-preservation of the evaporative fraction and the Bowen ratio. *Journal of Hydrology*, *178*, 241–255.

Demmig-Adams, B., & Adams, W. W. (1996). The role of xanthophyll cycle carotenoids in the protection of photosynthesis. *Trends in Plant Science*, *1*, 21–26.

dePury, D. G. G., & Farquhar, G. D. (1997). Simple scaling of photosynthesis from leaves to canopies without the errors of big-leaf models. *Plant Cell and Environment*, *20*, 537–557.

Dickinson, R. E., Shaikh, M., Bryant, R., & Graumlich, L. (1998). Interactive canopies for a climate model. *Journal of Climate*, *11*, 2823–2836.

Farquhar, G. D., Caemmerer, S. V., & Berry, J. A. (1980). A biochemical-model of photosynthetic CO_2 assimilation in leaves of C-3 species. *Planta*, *149*, 78–90.
Gamon, P. F. (1992). A narrow-waveband spectral index that tracks diurnal changes in photosynthetic efficiency. *Remote Sensing of Environment*, *41*, 35–44.
Garzoli, K., Blackwel, J., & Trickett, E. S. (1971). Heat-flux plate for use in soil. *Journal of Agricultural Engineering Research*, *16*, 420 (&).
Gomez-Chova, L., Alonso, L., Guanter, L., Camps-Valls, G., Calpe, J., & Moreno, J. (2008). Correction of systematic spatial noise in push-broom hyperspectral sensors: Application to CHRIS/PROBA images. *Applied Optics*, *47*, F46–F60.
Goulden, M. L., Munger, J. W., Fan, S. M., Daube, B. C., & Wofsy, S. C. (1996). Exchange of carbon dioxide by a deciduous forest: Response to interannual climate variability. *Science*, *271*, 1576–1578.
Hall, F. G., & Sellers, P. J. (1995). First International Satellite Land Surface Climatology Project (ISLSCP) Field Experiment (FIFE) in 1995. *Journal of Geophysical Research-Atmospheres*, *100*, 25383–25395.
Hall, F., Sellers, P. J., Strebel, D., Kanemasu, E., Kelly, R., Blad, B., et al. (1991). Satellite remote sensing of surface energy and mass balance results: Results from FIFE. *Remote Sensing of Environment*, *35*, 187–199.
Hall, F. G., Huemmrich, K. F., Goetz, S. J., Sellers, P. J., & Nickeson, J. E. (1992). Satellite remote-sensing of surface-energy balance — Success, failures, and unresolved issues in FIFE. *Journal of Geophysical Research-Atmospheres*, *97*, 19061–19089.
Hall, F. G., Hilker, T., Coops, N. C., Lyapustin, A., Huemmrich, K. F., Middleton, E., et al. (2008). Multi-angle remote sensing of forest light use efficiency by observing PRI variation with canopy shadow fraction. *Remote Sensing of Environment*, *112*, 3201–3211.
Hall, F. G., Hilker, T., & Coops, N. C. (2011). PHOTOSYNSAT, Photosynthesis from space: Theoretical foundations of a satellite concept and validation from tower and spaceborne data. *Remote Sensing of Environment*, *115*, 1918–1925.
Hall, F. G., Hilker, T., & Coops, N. C. (2012a). Data assimilation of photosynthetic light-use efficiency using multi-angular satellite data: I. *Model formulation. Remote Sensing of Environment*, *121*, 301–308.
Hall, F. G., Hilker, T., & Coops, N. C. (2012b). Data assimilation of photosynthetic light-use efficiency using multi-angular satellite data: I. Model formulation. *Remote Sensing of Environment*, *121*.
Hilker, T., Coops, N. C., Nesic, Z., Wulder, M. A., & Black, A. T. (2007). Instrumentation and approach for unattended year round tower based measurements of spectral reflectance. *Computers and Electronics in Agriculture*, *56*, 72–84.
Hilker, T., Coops, N. C., Schwalm, C. R., Jassal, R. S., Black, T. A., & Krishnan, P. (2008). Effects of mutual shading of tree crowns on prediction of photosynthetic light-use efficiency in a coastal Douglas-fir forest. *Tree Physiology*, *28*, 825–834.
Hilker, T., Coops, N. C., Coggins, S. B., Wulder, M. A., Brown, M., Black, T. A., et al. (2009). Detection of foliage conditions and disturbance from multi-angular high spectral resolution remote sensing. *Remote Sensing of Environment*, *113*, 421–434.
Hilker, T., Lyapustin, A., Hall, F. G., Wang, Y., Coops, N. C., Drolet, G., et al. (2009). An assessment of photosynthetic light use efficiency from space: Modeling the atmospheric and directional impacts on PRI reflectance. *Remote Sensing of Environment*, *113*, 2463–2475.
Hilker, T., Hall, F. G., Coops, N. C., Lyapustin, A., Wang, Y., Nesic, Z., et al. (2010). Remote sensing of photosynthetic light-use efficiency across two forested biomes: Spatial scaling. *Remote Sensing of Environment*, *114*, 2863–2874.
Hilker, T., Nesic, Z., Coops, N. C., & Lessard, D. (2010). A new, automated, multi-angular radiometer instrument for tower-based observation of canopy reflectance (AMSPEC II). *Instrumentation Science & Technology*, *38*, 319.
Hilker, T., Coops, N. C., Hall, F. G., Nichol, C. J., Lyapustin, A., Black, T. A., et al. (2011). Inferring terrestrial photosynthetic light use efficiency of temperate ecosystems from space. *Journal of Geophysical Research-Biogeosciences*, *116*.
Hilker, T., Hall, F. G., Black, T. A., Coops, N. C., Jassal, R., Mathys, A., et al. (2012). A new technique for estimating daytime respiration of forest ecosystems. *Global Biogeochemical Cycles* (under review).
Hilker, T., Hall, F. G., Tucker, C. J., Coops, N. C., Black, T. A., Nichol, C. J., et al. (2012). Data assimilation of photosynthetic light-use efficiency using multi-angular satellite data: II Model implementation and validation. *Remote Sensing of Environment*, *121*.
Hillel, D. (1998). *Environmental soil physics.* : Environmental soil physics.
Houborg, R. M., & Soegaard, H. (2004). Regional simulation of ecosystem CO_2 and water vapor exchange for agricultural land using NOAA AVHRR and Terra MODIS satellite data. Application to Zealand, Denmark. *Remote Sensing of Environment*, *93*, 150–167.
Jarvis, P. G. (1976). Interpretation of variations in leaf water potential and stomatal conductance found in canopies in field. *Philosophical Transactions of the Royal Society of London Series B-Biological Sciences*, *273*, 593–610.
Jassal, R. S., Black, T. A., Cai, T. B., Morgenstern, K., Li, Z., Gaumont-Guay, D., et al. (2007). Components of ecosystem respiration and an estimate of net primary productivity of an intermediate-aged Douglas-fir stand. *Agricultural and Forest Meteorology*, *144*, 44–57.
Kidston, J., Brummer, C., Black, T. A., Morgenstern, K., Nesic, Z., McCaughey, J. H., et al. (2010). Energy balance closure using eddy covariance above two different land surfaces and implications for CO(2) flux measurements. *Boundary-Layer Meteorology*, *136*, 193–218.
Leuning, R. (1990). Modeling stomatal behavior and photosynthesis of *Eucalyptus-grandis*. *Australian Journal of Plant Physiology*, *17*, 159–175.
Ma, J. L., Chan, J. C. W., & Canters, F. (2010). Fully automatic subpixel image registration of multiangle CHRIS/Proba data. *IEEE Transactions on Geoscience and Remote Sensing*, *48*, 2829–2839.
Margolis, H. A., Flanagan, L. B., & Amiro, B. D. (2006). The Fluxnet-Canada Research Network: Influence of climate and disturbance on carbon cycling in forests and peatlands. *Agricultural and Forest Meteorology*, *140*, 1–5.
Monteith, J. L. (1972). Solar-radiation and productivity in tropical ecosystems. *Journal of Applied Ecology*, *9*, 747–766.
Monteith, J. L. (1973). *Principles of environmental physics.* London: Edward Arnold.
Monteith, J. L., & Unsworth, M. H. (1990). *Principles of environmental physics, second edition.* (Monteith, J. L. and M. H. Unsworth. Principles of Environmental Physics, Second Edition. Xii+291 pp. New York, New York, USA. Illus. Paper, XII + 291P).
Morgenstern, K., Black, T. A., Humphreys, E. R., Griffis, T. J., Drewitt, G. B., Cai, T. B., et al. (2004). Sensitivity and uncertainty of the carbon balance of a Pacific Northwest Douglas-fir forest during an *El Nino La Nina* cycle. *Agricultural and Forest Meteorology*, *123*, 201–219.
Norman, J. M., Anderson, M. C., Kustas, W. P., French, A. N., Mecikalski, J., Torn, R., et al. (2003). Remote sensing of surface energy fluxes at 10(1)-m pixel resolutions. *Water Resources Research*, *39*.
Piper, S. C. (1995). *Construction and description of a gridded global dataset of daily temperature and precipitation for terrestrial biospheric modelling. Scripps Institution of Oceanography*, University of California, (134pages).
Schaefer, K., Schwalm, C. R., Williams, C., Arain, M. A., Barr, A., Chen, J. M., et al. (2012). A model-data comparison of gross primary productivity: Results from the North American Carbon Program site synthesis. *Journal of Geophysical Research-Biogeosciences*, *117*.
Sellers, P. J., Heiser, M. D., & Hall, F. G. (1992). Relations between surface conductance and spectral vegetation indexes at intermediate ($100m^2$ to $15km^2$) length scales. *Journal of Geophysical Research-Atmospheres*, *97*, 19033–19059.
Sellers, P. J., Los, S. O., Tucker, C. J., Justice, C. O., Dazlich, D. A., Collatz, G. J., et al. (1996). A revised land surface parameterization (SiB2) for atmospheric GCMs. 2. The generation of global fields of terrestrial biophysical parameters from satellite data. *Journal of Climate*, *9*, 706–737.
Sellers, P. J., Randall, D. A., Collatz, G. J., Berry, J. A., Field, C. B., Dazlich, D. A., et al. (1996). A revised land surface parameterization (SiB2) for atmospheric GCMs .1. model formulation. *Journal of Climate*, *9*, 676–705.
Sellers, P. J., Hall, F. G., Kelly, R. D., Black, A., Baldocchi, D., Berry, J., et al. (1997). Boreas in 1997: Experiment overview, scientific results, and future directions. *Journal of Geophysical Research-Atmospheres*, *102*, 28731–28769.
Sugita, M., & Brutsaert, W. (1991). Daily evaporation over a region from lower boundary-layer profiles measured with radiosondes. *Water Resources Research*, *27*, 747–752.
Thuillier, G., Herse, M., Labs, D., Foujols, T., Peetermans, W., Gillotay, D., et al. (2003). The solar spectral irradiance from 200 to 2400 nm as measured by the SOLSPEC spectrometer from the ATLAS and EURECA missions. *Solar Physics*, *214*, 1–22.